Model-Based Reconstruction for Real-Time Phase-Contrast Flow MRI: Improved Spatiotemporal Accuracy

Zhengguo Tan,[1]* Volkert Roeloffs,[1] Dirk Voit,[1] Arun A. Joseph,[1,2] Markus Untenberger,[1] K. Dietmar Merboldt,[1] and Jens Frahm[1,2]

Purpose: To develop a model-based reconstruction technique for real-time phase-contrast flow MRI with improved spatiotemporal accuracy in comparison to methods using phase differences of two separately reconstructed images with differential flow encodings.

Methods: The proposed method jointly computes a common image, a phase-contrast map, and a set of coil sensitivities from every pair of flow-compensated and flow-encoded datasets obtained by highly undersampled radial FLASH. Real-time acquisitions with five and seven radial spokes per image resulted in 25.6 and 35.7 ms measuring time per phase-contrast map, respectively. The signal model for phase-contrast flow MRI requires the solution of a nonlinear inverse problem, which is accomplished by an iteratively regularized Gauss-Newton method. Aspects of regularization and scaling are discussed. The model-based reconstruction was validated for a numerical and experimental flow phantom and applied to real-time phase-contrast MRI of the human aorta for 10 healthy subjects and 2 patients.

Results: Under all conditions, and compared with a previously developed real-time flow MRI method, the proposed method yields quantitatively accurate phase-contrast maps (i.e., flow velocities) with improved spatial acuity, reduced phase noise and reduced streaking artifacts.

Conclusion: This novel model-based reconstruction technique may become a new tool for clinical flow MRI in real time.

Key words: nonlinear inverse reconstruction; model-based reconstruction; cardiovascular blood flow; phase-contrast flow MRI; radial MRI; real-time MRI

INTRODUCTION

Based on the physical relationship between a gradient-induced phase shift and the velocity of spins in a corresponding NMR (1) or MRI experiment (2) as well as initiated by early seminal applications (3–5), there is nowadays extensive clinical use of velocity-encoded phase-contrast techniques for quantitative MRI studies of blood flow. For relevant reviews see (6,7). More recently, technical advances in real-time MRI (8), which rely on regularized nonlinear inverse (NLINV) reconstructions of highly undersampled radial gradient-echo acquisitions (9–12), have been extended to cardiovascular applications (13–15) and, in particular, to phase-contrast flow MRI (16–18). These and other accelerated flow MRI studies (19,20) combine parallel imaging with a phase-difference computation (21) of two complex images with complementary velocity encodings, e.g., a flow-compensated and a flow-encoded acquisition. As a consequence, phase-difference maps present with extensive phase noise in areas of low or no MRI signal (e.g., air). Although tolerable in many cases, the presence of strong noise may complicate the definition of the true vessel lumen and, therefore, affect quantitative flow analyses, hamper the assessment of flow in small vessels or, in case of radial undersampling, enhance residual streaking artifacts.

On the other hand, model-based approaches in MRI are a well-introduced concept for a variety of postprocessing problems, e.g., image segmentation. However, less attention has been paid to model-based reconstructions, despite the fact that respective techniques have previously been detailed in an excellent review (22). While selected proposals deal with accelerated T2 mapping (23–25), fat-water imaging (26), inhomogeneity-corrected T2* mapping (27), quantitative susceptibility mapping (28) and reconstructions of the diffusion tensor (29), preliminary attempts have also been made to use constrained reconstruction techniques for accelerated phase-contrast flow MRI (30,31). For example, Kwak et al. (30) reconstructed flow-compensated and flow-encoded images by regularizing the sparsity of the complex-difference image (21). Alternatively, Sun et al. (31) recently used the complex difference of the acquired raw data in k-space directly as part of a signal model. However, before the final calculation of the desired phase-contrast (i.e., velocity) map, both approaches still require the initial reconstruction of either the flow-compensated and flow-encoded image, or the flow-compensated and complex-difference image, and, therefore, do not offer a direct reconstruction of a phase-contrast velocity map.

In contrast, the present work proposes a model-based reconstruction technique for phase-contrast flow MRI

[1]Biomedizinische NMR Forschungs GmbH am Max-Planck-Institut für biophysikalische Chemie, Göttingen, Germany.
[2]DZHK, German Center for Cardiovascular Research, partner site Göttingen, Germany.
*Correspondence to: Zhengguo Tan, M.Sc., Biomedizinische NMR Forschungs GmbH am Max-Planck-Institut für biophysikalische Chemie, 37070 Göttingen, Germany. E-mail: ztan@gwdg.de

Received 6 November 2015; revised 9 February 2016; accepted 9 February 2016
DOI 10.1002/mrm.26192
Published online 7 March 2016 in Wiley Online Library (wileyonlinelibrary.com).

that jointly computes a complex image, a phase-contrast velocity map, and a set of coil sensitivities from every pair of flow-compensated and flow-encoded datasets. In particular, this initial description of a novel technique focuses on real-time flow MRI applications where respective datasets represent extremely undersampled gradient-echo acquisitions (18) that allow for monitoring blood flow at very high temporal resolution. Real-time phase-contrast flow MRI thus refers to high-speed MRI acquisitions at millisecond resolution as opposed to electrocardiogram-synchronized MRI acquisitions which extend over multiple cardiac cycles. The formulation of the nonlinear inverse reconstruction problem for the proposed signal model leads to an iterative solution which directly offers a quantitatively accurate phase-contrast map with improved spatial accuracy and much reduced phase noise. At this stage, however, and in contrast to a previous real-time phase-contrast flow MRI technique (18), the numerical solution has been developed offline for retrospective analysis.

THEORY

Model-based Reconstruction

Assuming the same magnitude image and the same coil sensitivities for each pair ($l = 1, 2$) of flow-compensated and flow-encoded datasets, the phase-contrast flow MRI signal can be written as

$$y_{j,l}(t) = \int \rho(\vec{x}) \cdot e^{z(\vec{x})\cdot S_l} \cdot c_j(\vec{x}) \cdot e^{i\vec{k_l}(t)\vec{x}} d\vec{x} \quad \text{with} \quad j \in [1, N],\ l \in [1, 2]. \qquad [1]$$

Here, ρ is the complex image shared by the flow-compensated and flow-encoding acquisition, z denotes a complex map which contains the phase differences $\Delta\phi$ in its imaginary part, while the real part is constrained to be zero, c_j is the sensitivity map of the j^{th} coil, and $\vec{k}_l(t)$ is the k-space sampling trajectory of the l^{th} acquisition. The indices $S_1 = 0$ and $S_2 = 1$ represent the flow-compensated and flow-encoded acquisition, respectively. The unknowns ρ, z, and c_j in this nonlinear signal model can be solved by the iteratively regularized Gauss-Newton method (32,33) as previously introduced for NLINV (8,9). It estimates the minimum of the cost function

$$\Phi(x) = ||y - F(x)||_2^2 \text{ with } x = \begin{pmatrix} \rho \\ z \\ c_1 \\ \vdots \\ c_N \end{pmatrix} \qquad [2]$$

Here, x is the unknowns and y is the measured k-space data. According to Eq. [1] the forward operator F is

$$F : x \mapsto \begin{pmatrix} P_1 \cdot \mathcal{F}\{\rho \cdot e^{z\cdot 0} \cdot c_1\} \\ \vdots \\ P_1 \cdot \mathcal{F}\{\rho \cdot e^{z\cdot 0} \cdot c_N\} \\ P_2 \cdot \mathcal{F}\{\rho \cdot e^{z\cdot 1} \cdot c_1\} \\ \vdots \\ P_2 \cdot \mathcal{F}\{\rho \cdot e^{z\cdot 1} \cdot c_N\} \end{pmatrix} \qquad [3]$$

with $\mathcal{F}$ the discrete Fourier transform and P_l the orthogonal projection onto the l^{th} trajectory. In this study, the forward operation on the j^{th} coil of the l^{th} acquisition is denoted as

$$F_{j,l}(x) = P_l \cdot \mathcal{F}\{\rho \cdot e^{z\cdot S_l} \cdot c_j\}.$$

Due to the nonlinearity of this forward operator, the iteratively regularized Gauss-Newton method (32,33) firstly linearizes the model around the estimate x_n from the n^{th} Newton step, which yields

$$F(x_n + dx) \approx F(x_n) + DF(x_n)dx$$

with $DF(x)$ the Frechét derivative. Thus, the cost function in Eq. [2] becomes

$$\Phi(dx) = ||[y - F(x_n)] - DF(x_n)dx||_2^2,$$

which can be solved with use of the conjugate gradient method. By adding Tikhonov regularization similar to (9,10), the cost function of the linearized model is

$$\Phi(dx) = ||DF(x_n)dx - [y - F(x_n)]||_2^2 + \alpha_n||x_n + dx - p \cdot x_0||_2^2 \qquad [4]$$

with p the damping factor, α_n the Tikhonov regularization parameter which decreases in every Newton step, and x_0 the initial guess. To solve this problem, two further operators are needed. The first operator is the Frechét derivative of the forward operator $DF(x)$, which can be calculated by applying the Jacobian matrix and the linear property of the Fourier transform to F. Take $F_{j,l}$ as an example,

$$DF_{j,l}(x) \begin{pmatrix} d\rho \\ dz \\ dc_1 \\ \vdots \\ dc_N \end{pmatrix} = P_l\mathcal{F}\{e^{z\cdot S_l}(c_j \cdot d\rho + S_l\rho \cdot c_j \cdot dz + \rho \cdot dc_j)\} = dy_{j,l} \qquad [5]$$

where the product of $DF(x)$ and dx maps dx to dy. The second operator is the adjoint of the Frechét derivative $DF^H(x)$, which can be derived using the unitary property of $\mathcal{F}$,

$$DF^H(x)\begin{pmatrix} dy_{1,1} \\ \vdots \\ dy_{N,1} \\ dy_{1,2} \\ \vdots \\ dy_{N,2} \end{pmatrix} = \begin{pmatrix} \sum_{j=1}^{N} c_j^* \cdot \left[\sum_{l=1}^{2} \left(e^{z\cdot S_l}\right)^* \cdot \mathcal{F}^{-1}\{P_l^H \cdot dy_{j,l}\}\right] \\ \Im\left(\sum_{j=1}^{N} c_j^* \cdot \left[\sum_{l=1}^{2} S_l \cdot \left(e^{z\cdot S_l}\right)^* \cdot \rho^* \cdot \mathcal{F}^{-1}\{P_l^H \cdot dy_{j,l}\}\right]\right) \\ \sum_{l=1}^{2} \left(e^{z\cdot S_l}\right)^* \cdot \rho^* \cdot \mathcal{F}^{-1}\{P_l^H \cdot dy_{1,l}\} \\ \vdots \\ \sum_{l=1}^{2} \left(e^{z\cdot S_l}\right)^* \cdot \rho^* \cdot \mathcal{F}^{-1}\{P_l^H \cdot dy_{N,l}\} \end{pmatrix} \quad [6]$$

where $*$ denotes the point-wise complex conjugation and $\Im$ is the imaginary part of dz. The imaginary constraint is necessary due to the assumption that the flow-compensated and flow-encoded datasets only differ in their phases. With the two operators derived above, the solution to Eq. [4] is

$$dx = [DF(x_n)^H DF(x_n) + \alpha_n I]^{-1}\{DF(x_n)^H[y - F(x_n)] + \alpha_n(x_0 - x_n)\}. \quad [7]$$

Scaling

When using first derivatives in a model-based iterative reconstruction of multiple parameters, the relative scaling of parameters should be considered to balance the L^2 norm among all partial derivatives. A proper scaling accelerates the iterative optimization process, while maintaining quantitative accuracy, e.g., see (23–25). For the model-based reconstruction of phase-contrast flow MRI data as proposed here, scaling was accomplished by introducing the index $\hat{S}_l$: $\hat{S}_l = s \cdot S_l$, so that the estimated phase-difference map becomes

$$\hat{z} = z/s \quad [8]$$

with s being a scalar. From Eq. [6] the following property can be derived using $\hat{z}\cdot\hat{S}_l = z \cdot S_l$,

$$d\hat{z} \propto \hat{S}_l. \quad [9]$$

Although s may heuristically be selected (23), this work uses an automatic mechanism which takes advantage of Eq. [9] to derive the scaling. It is accomplished by exploiting the complex-difference image (21)

$$|\rho_1 - \rho_2| = M \cdot \sqrt{2[1 - \cos(\Delta\phi)]} \quad [10]$$

where $M = |\rho_1| = |\rho_2|$. It can then be proven to hold for relatively small phase-differences

$$||\sqrt{2 \cdot [1 - \cos(\Delta\phi)]}||_2 \approx ||\Delta\phi||_2. \quad [11]$$

When normalizing ρ_1 and ρ_2 by $||M||_2$ and taking the L^2 norm of both sides, Eq. [10], i.e., the relation between the norm of the complex-difference and that of the phase-difference image, can be reformulated using Eq. [11]

$$||(\rho_1 - \rho_2)/||M||_2||_2 \approx ||\Delta\phi||_2. \quad [12]$$

The norm of the complex-difference in image space is equivalent to that in k-space, so the left-hand side of Eq. [12] can be estimated from the gridded multi-channel k-space data of the flow-compensated and flow-encoded acquisitions y_1 and y_2, respectively,

$$s = 0.5 \cdot (||y_1||_2 + ||y_2||_2)/||y_1 - y_2||_2 \approx 1/||\Delta\phi||_2 \quad [13]$$

where the scalar s directly quantifies the intensity ratio between the magnitude image and phase-difference map and 1 indicates the norm of the normalized magnitude image. The scaling mechanism by means of the scalar s not only balances the derivatives, but also ensures a proper balance between the data consistency term and the regularization term in Eq. [4] because the regularization of z is implicitly controlled by s (see Eq. [8]).

Because real-time phase-contrast flow MRI is a dynamic process, serial phase-difference maps (as well as complex-difference images) may lead to different scaling values as determined by Eq. [13]. This variation is shown in Figure 1 for experimental data of the human aorta (gray line). While s can be as large as 10 in case of very low phase-difference values, i.e., in the absence of flow, such large values should be avoided as they decrease the regularization strength and accumulate noise in the final estimate. Therefore, the following steps are taken to dynamically determine the effective scaling. Starting with a value of 5, s is calculated from Eq. [13] for each frame and continuously updated by any lower scaling. For studies of human blood flow this typically means that s decreases until the real-time flow MRI acquisition reaches the first systole (compare Figure 1, black line), so that quantitative analyses of real-time flow MRI studies may eliminate the first cardiac cycle.

Regularization

As shown in Eq. [4], Tikhonov regularization is used for the solution of the linear problem with α_n a tunable regularization parameter, which starts with 1 and decreases in each Newton step by a factor of 2. In this study, α_n is

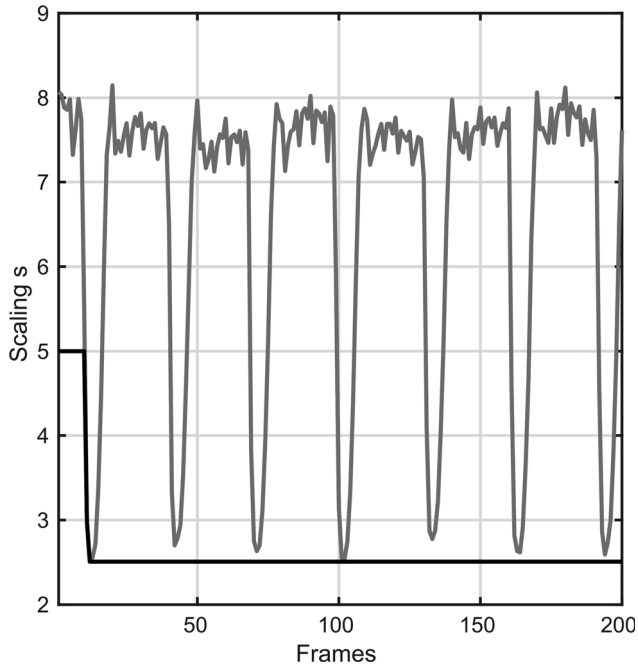

FIG. 1. Scaling values *s* for real-time phase-contrast flow MRI (35.7 ms resolution) of the aorta of a healthy subject: Gray line = according to Eq. [13], black line = used for serial model-based reconstructions.

identical among all parameters. In addition, the model-based image reconstruction adopts the L^2-norm regularization on the high spatial frequencies of the coil sensitivity maps as used for NLINV (8–10,16–18), and uses a temporal regularization of the current set of model parameters (i.e., maps) with the respective maps of the immediately preceding pair of datasets damped by a factor of 0.7. The reconstruction of the very first maps is initialized using $\rho = 1$, $z = 0$, and $c_j = 0$.

The radial sampling pattern has a circular field-of-view and thus encodes no information in the corners of k-space. As a result, high spatial frequency signals, which may appear as checkerboard artifacts in image domain, have the freedom to accumulate during model-based reconstruction. To avoid this problem, a k-space filter (34) is added to the sampling pattern *P* which penalizes signals in the undefined corners of k-space.

Pre- and Postprocessing

Before the iterative optimization, the datasets from multiple receiver coils are first corrected for gradient delay errors (18), and then compressed to 10 virtual coils by a principle component analysis. This latter process must apply the same transformation matrix on both the flow-compensated and the flow-encoded datasets. Finally, the data and the sampling trajectories are interpolated onto Cartesian grids without density compensation, which is not required for a nonlinear inverse reconstruction of gridded radial data (10). After solving the nonlinear inverse problem, the final complex phase-contrast maps are given by

$$\rho_{PC} = |\rho| \cdot e^{i \cdot s \cdot \Im(z)}. \quad [14]$$

METHODS

Numerical Flow Phantom

To ensure the quantitative accuracy of the proposed reconstruction method, a numerical flow phantom was built with superimposed ellipses, whose analytical Fourier transform is known and can be evaluated at given k-space trajectories. Moreover, 10 receiver coils were simulated based on the Biot-Savart law and sinusoidal fitting (35). To mimic phase-contrast flow MRI, the simulation included one flow-compensated and one flow-encoded acquisition with the same magnitude signal strengths. The simulated ellipses had zero phase in the flow-compensated acquisition, while phase values of 150°, -100°, and -15° were added to the three ellipses in the flow-encoded acquisition to represent different velocities and directions. The simulations were performed for datasets with 45, 15, 7, and 5 radial spokes (symmetric echoes, base resolution 170 pixels) each covering a view angle of 360°. Serial datasets used interleaved spokes in five successive acquisitions similar to experimental conditions. Complex white Gaussian noise with a standard deviation of 0.1 was added to the data, so that the signal-to-noise ratio decreased with the number of spokes. While model-based image reconstructions of numerical phantoms based on analytical Fourier transform usually suffer from aliasing artifacts, these may be suppressed by decreasing the Tikhonov regularization parameter or by adjusting the sampling pattern (24). Here, a damping factor of 1 for the *z* map was only used for reconstructions of the numerical flow phantom.

Real-Time Phase-Contrast Flow MRI

This work presents real-time flow MRI data of the ascending (and descending) aorta obtained at 3 Tesla (T) (Magnetom Prisma, Siemens Healthcare, Erlangen, Germany). The analyses include five volunteers without known illness and two patients with combined aortic valve insufficiency and partial stenosis previously studied with "conventional" real-time flow MRI (18) as well as new experimental data from five additional healthy subjects. All subjects gave written informed consent before MRI in compliance with the regulations established by the local ethics committee.

Real-time phase-contrast flow MRI was based on extremely undersampled radial FLASH MRI (five or seven spokes per image) with asymmetric gradient echoes (18) using two sequential acquisitions of a dataset with velocity-compensated gradients in all gradient axes and with velocity-encoding of through-plane flow, respectively. While studies of the experimental flow phantom (VENC = 200 cm s^{-1}) used the 64-channel head coil, blood flow in the human aorta (VENC = 200 to 400 cm s^{-1}) was studied during free breathing by combining an 18-element thorax coil with 32 elements of the spine coil. Acquisitions [repetition time/echo time (TR/TE) = 2.38/1.59 ms, flip angle 10°] of the previously described flow phantom (18) were performed at 1.4 mm

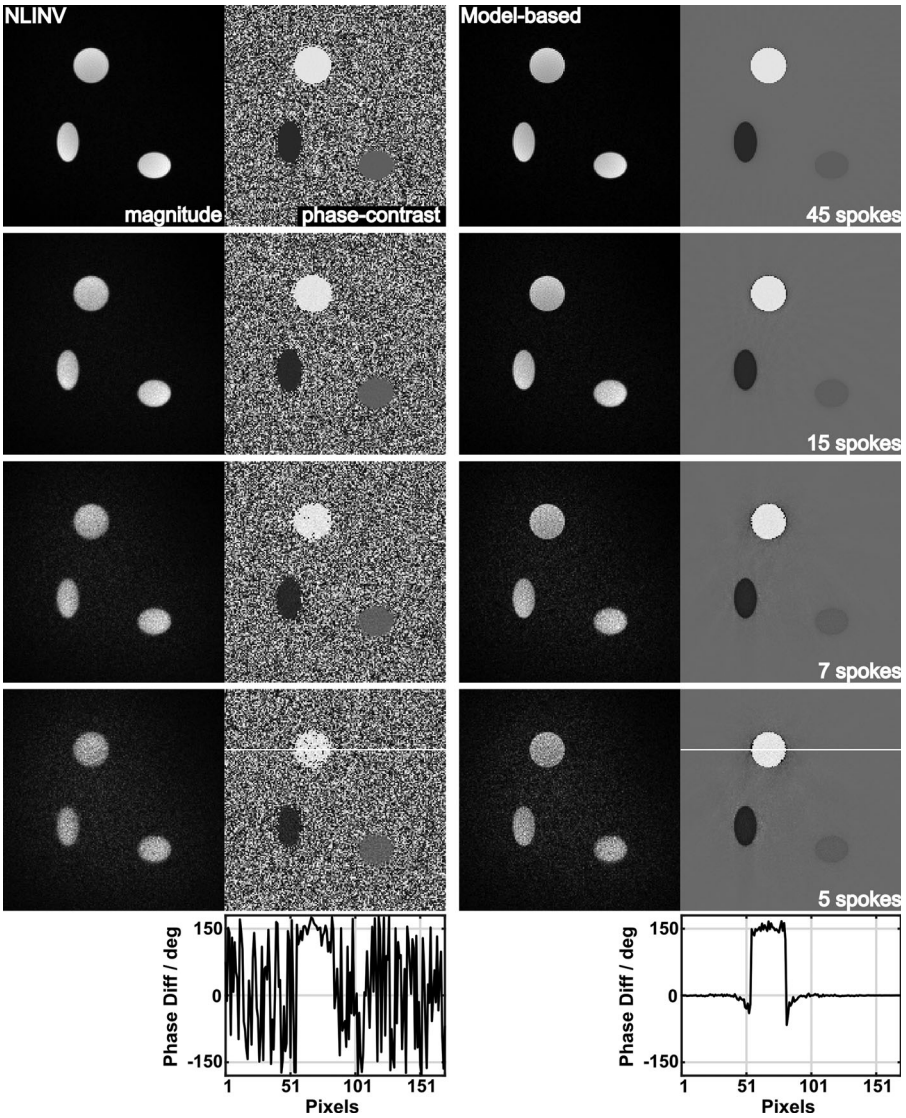

FIG. 2. NLINV (left) and model-based (right) reconstructions of magnitude images and phase-contrast maps as well as phase-difference profiles (along indicated reference lines) for a numerical flow phantom (complex white Gaussian noise, standard deviation 0.1) and constant flow in three ellipses corresponding to phase values of 150°, -100°, and -15°. The results were obtained for simulated acquisitions with 45, 15, 7, and 5 spokes (see Table 1). The Gibbs ringing artifact around the 150° ellipse in phase-contrast maps stems from the numerical design of the phantom. It is less well visible in NLINV reconstructions because of the phase noise for zero-flow pixels.

in-plane resolution (192 mm field-of-view, 6 mm slice thickness) and 33.32 ms temporal resolution (7 spokes for the flow-encoded and flow-compensated image, respectively). All in vivo measurements (TE = 1.70 ms, flip angle 10°) had 1.5 mm in-plane resolution, 320 mm field-of-view, 6 mm slice thickness, and 35.7 ms (2×7 spokes, TR = 2.55 ms) or 25.6 ms temporal resolution (2×5 spokes, TR = 2.56 ms) corresponding to 28 or 39 frames per second (fps), respectively. For both NLINV and model-based reconstructions, the serial magnitude images were subject to a temporal median filter, whereas no temporal filter was applied to phase-contrast maps.

Online reconstruction and display of real-time NLINV images was achieved by a parallelized version of the NLINV algorithm (11) and a bypass computer (sysGen/TYAN Octuple-GPU, Sysgen, Bremen, Germany) equipped with two processors (CPUs, SandyBridge E5-2650, Intel, Santa Clara, CA) and eight graphics processing units (TITAN, NVIDIA, Santa Clara, CA). The system was fully integrated into the reconstruction pipeline of the commercial MRI system. Depending on image matrix (i.e., resolution and/or FOV) the current reconstruction speed ranges from 6 to 14 fps (i.e., magnitude images and phase-contrast maps). At this stage, model-based reconstructions were implemented on a single graphics processing unit (GeForce GTX 580, NVIDIA, Santa Clara, CA) and performed offline after data acquisitions. Typically, the current implementation takes approximately 4.5 s per frame.

Quantitative analyses of phase-contrast flow MRI data were obtained with the use of CAIPI prototype software (Fraunhofer MEVIS, Bremen, Germany), especially modified for the automated analysis of real-time MRI data, i.e., vessel or myocardial segmentation throughout the entire time series without the need for manual corrections (36).

RESULTS

Validation Studies

To assess the quantitative reliability of the model-based phase-contrast flow MRI technique, the mathematical

approach was validated with the use of a numerical flow phantom providing ground truth in the presence of noise. Figure 2 compares the results obtained for NLINV reconstructions with subsequent calculation of a phase-difference map and direct model-based reconstructions for simulations with a decreasing number of spokes per image. For high degrees of undersampling, the model-based phase-contrast maps present with visibly better signal-to-noise ratio and sharper "vessel" definition. The quantitative analyses in Table 1 confirm the excellent accuracy of phase (i.e., velocity) values obtained by the proposed model-based reconstruction, even for acquisitions with only seven or five spokes per image. Most importantly, this not only applies to mean values, but also to the standard deviations which for highly undersampled acquisitions are much smaller than for NLINV-based reconstructions.

Similarly, Figure 3 shows the results for an experimental phantom providing constant flow at two different velocities (i.e., depending on tube diameter) and two opposing flow directions (forward versus backward flow). Again, the most apparent feature is the almost noise-less appearance of the model-based phase-contrast map which benefits from the a priori knowledge of zero phase for all pixels without flow or no MRI signal. In contrast, all "conventional" flow MRI techniques, which rely on the phase-difference calculation of two independent complex images with differential flow encodings, yield arbitrary phase values (and corresponding phase differences) in zero-signal pixels as well as some tissue-dependent phase in pixels with stationary signal. In relation to this advantageous zero-phase property,

Table 1
Quantitative Flow Evaluations for a Numerical Flow Phantom[a]

Spokes per image	True phase difference	NLINV[b] reconstruction	Model-based[c] reconstruction
	150	150.0 ± 1.7	150.1 ± 1.4
45	−100	−100.0 ± 1.4	−100.2 ± 1.0
	−15	−15.0 ± 1.3	−15.1 ± 0.6
	150	150.0 ± 5.5	149.8 ± 2.5
15	−100	−100.0 ± 5.2	−100.2 ± 2.3
	−15	−15.0 ± 4.4	−15.0 ± 1.6
	150	146.4 ± 36.0	149.6 ± 5.7
7	−100	−100.8 ± 12.0	−102.7 ± 5.3
	−15	−15.6 ± 10.6	−15.5 ± 3.1
	150	131.7 ± 73.8	150.6 ± 8.8
5	−100	−101.6 ± 18.6	−103.8 ± 6.5
	−15	−15.4 ± 14.5	−15.9 ± 3.7

[a]Results represent mean values ± standard deviation.
[b]NLINV reconstructions with subsequent calculation of a phase-difference map.
[c]Direct model-based reconstruction of phase-contrast map.

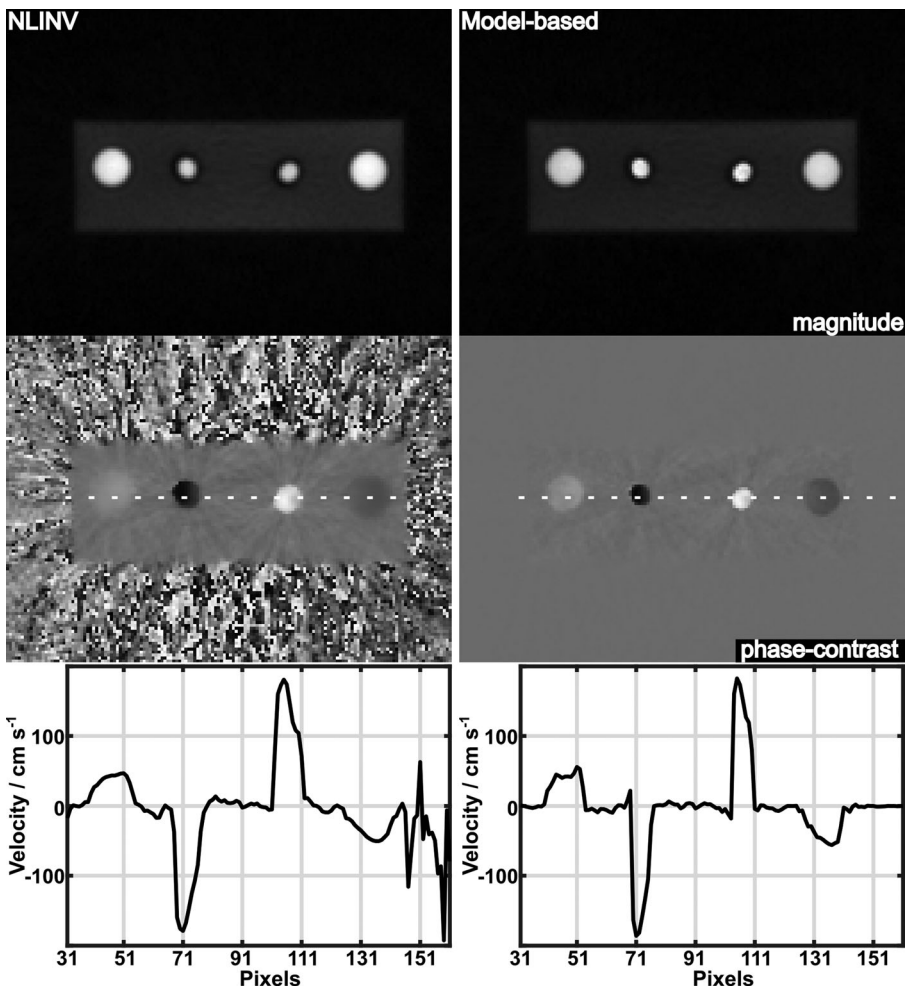

FIG. 3. NLINV (left) and model-based (right) reconstructions of magnitude images (top) and phase-contrast maps (middle) as well as velocity profiles (along indicated reference lines) for an experimental flow phantom with constant (bidirectional) flow (tubes 1 to 4 from left to right, compare Table 2). The results were obtained for real-time phase-contrast flow MRI at 33.3 ms resolution and VENC = 200 cm s^{-1}. Residual streaking artifacts in the NLINV phase-contrast map are reduced in the model-based reconstruction which further improves the spatial definition of all tubes (compare Table 2).

Table 2
Quantitative Evaluations of an Experimental Flow Phantom

Tube[a]	Method	Tube size magnitude image[b] mm^2	Tube size phase-contrast map mm^2	Peak velocity $cm\ s^{-1}$	Flow volume[c] $L\ min^{-1}$
1	NLINV	255	360	55	6.5
	Model-based	239	243	63	6.8
2	NLINV	76	131	− 189	− 7.3
	Model-based	71	75	− 180	− 6.5
3	NLINV	78	139	181	6.9
	Model-based	73	75	185	6.9
4	NLINV	255	302	− 52	− 7.0
	Model-based	235	233	− 58	− 6.8

[a]Tubes 1 to 4 are shown in Fig. 3 from left to right.
[b]Estimated sizes from high-resolution MRI are about 250 mm^2 (tubes 1, 4) and 70 mm^2 (tubes 2, 3), respectively.
[c]The flow volume as determined by a flow meter was 6.3 $L\ min^{-1}$.

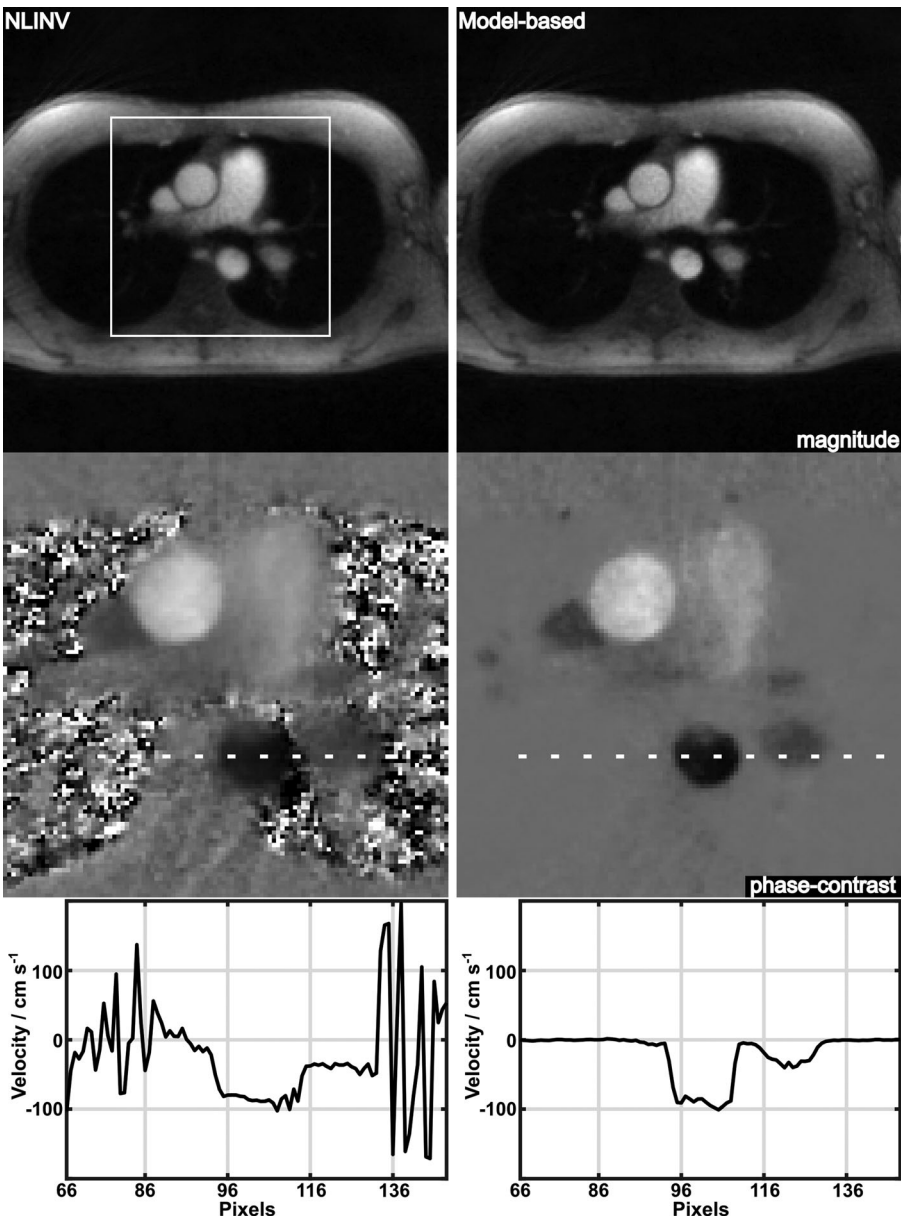

FIG. 4. NLINV (left) and model-based (right) reconstructions of systolic magnitude images and phase-contrast maps (magnified views) (top) as well as velocity profiles (along indicated reference lines) for real-time phase-contrast MRI of aortic blood flow in a healthy volunteer at 35.7 ms resolution and VENC = 200 $cm\ s^{-1}$.

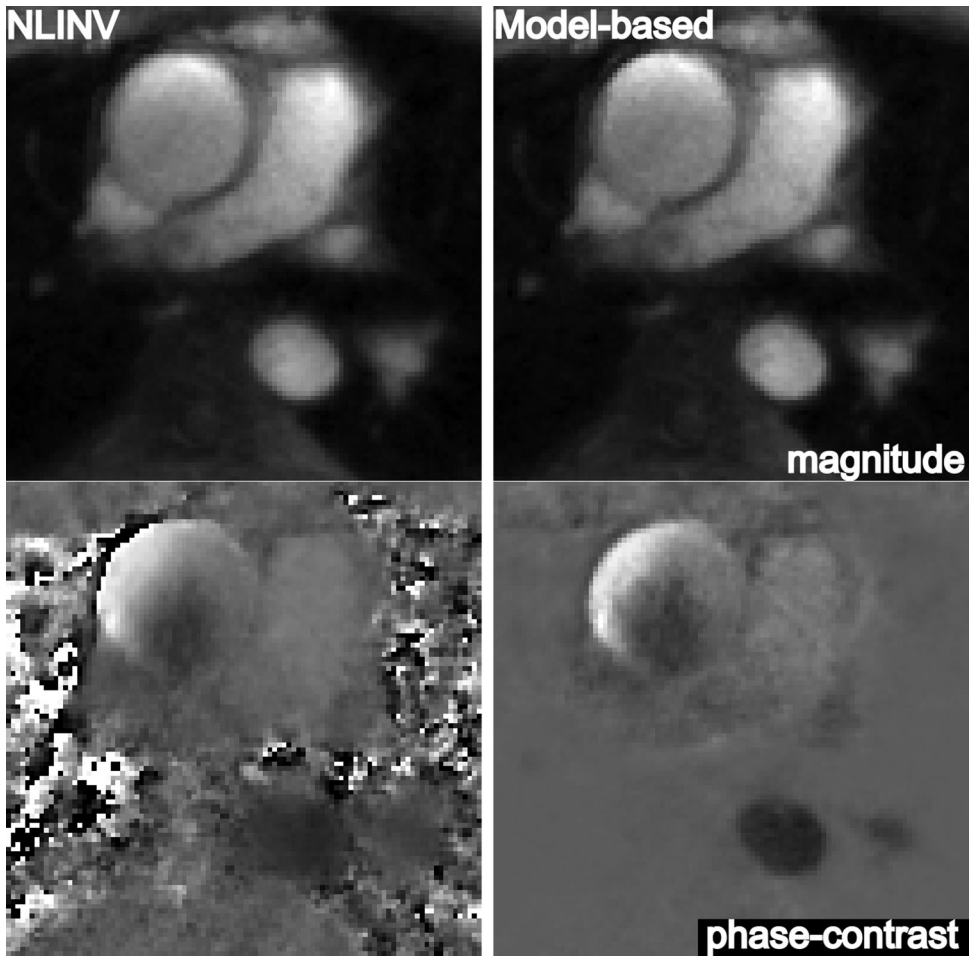

FIG. 5. NLINV (left) and model-based (right) reconstructions of systolic magnitude images (top) and phase-contrast maps (bottom) (magnified views) for real-time phase-contrast MRI of a patient with aortic valve insufficiency and partial stenosis at 35.7 ms resolution and VENC = 400 cm s^{-1}.

which is effective as an additional constraint, the model-based reconstruction reduces the strength of residual streakings extending from the high-flow tubes in the phase-contrast maps shown in Figure 3.

Most importantly, however, model-based phase-contrast maps yield a spatially much more accurate definition of the flow signal (i.e., vessel lumen) than obtainable by conventional NLINV reconstructions. In fact, the spatial information of the model-based phase-contrast map in Figure 3 precisely matches the magnitude image information, whereas flow areas in NLINV phase-contrast maps are larger compared with both the true lumen sizes. These qualitative observations are confirmed by quantitative analyses summarized in Table 2. In contrast to NLINV, model-based reconstructions not only yield almost identical flow areas in magnitude images and phase-contrast maps, but are also in close agreement with estimates of tube sizes as obtained by high-resolution MRI. Nevertheless, flow evaluations reveal good agreement between both flow MRI methods with respect to peak velocity as a direct (although focal) result of the phase-contrast determination, while flow volumes tend to be slightly larger than a determination by a flow meter.

Human Studies

Qualitative comparisons of NLINV and model-based phase-contrast MRI are depicted in Figure 4 for a normal subject and in Figure 5 for a patient with aortic valve insufficiency and partial stenosis (Supporting Videos S1 and S2, which are available online), respectively. In line with results for the experimental flow phantom, the systolic phase-contrast maps obtained by the model-based reconstruction yield a much better spatial definition in regions with non-zero flow (i.e., vessels). Here, this particularly applies to the descending aorta whose phase-difference presentation is in close agreement with the vessel lumen in the magnitude image. In quantitative terms, the analysis of peak systolic frames from 10 consecutive heartbeats of the subject shown in Figure 4 revealed $445 \pm 16\,mm^2$ ($781 \pm 20\,mm^2$) for the lumen of the descending (ascending) aorta in model-based phase-contrast maps versus $569 \pm 41\,mm^2$ ($880 \pm 18\,mm^2$) for NLINV reconstructions.

In addition, the implicit a priori knowledge of zero phase in pixels without flowing spins precludes the iterative optimization process to generate residual streaking artifacts in areas around vessels with maximum systolic flow, i.e., for signals with high temporal and spatial frequencies that are most severely affected by k-space undersampling. Quantitative results for both NLINV and model-based reconstructions are summarized in Table 3 for five subjects and two patients studied previously (18) and found to be in general agreement. In comparison to Untenberger et al. (18) all analyses were performed with

Table 3
Quantitative Flow Evaluations of the Ascending Aorta of Healthy Volunteers and Patients With Valve Insufficiency[a]

Subject	Reconstruction technique	Peak velocity cm s^{-1}	Flow per heartbeat mL	Flow volume L min^{-1}	Regurgitation fraction %
1	NLINV	120 ± 3	99 ± 4	5.7 ± 0.4	2 ± 1
	Model-based	121 ± 4	91 ± 5	5.2 ± 0.4	1 ± 1
2	NLINV	114 ± 8	124 ± 6	6.9 ± 0.3	1 ± 1
	Model-based	114 ± 7	112 ± 5	6.3 ± 0.2	1 ± 1
3	NLINV	69 ± 3	61 ± 3	4.0 ± 0.2	2 ± 1
	Model-based	76 ± 4	62 ± 2	4.1 ± 0.2	1 ± 1
4	NLINV	112 ± 5	131 ± 4	8.1 ± 0.3	2 ± 1
	Model-based	111 ± 4	123 ± 4	7.6 ± 0.3	2 ± 1
5	NLINV	100 ± 5	107 ± 3	6.2 ± 0.1	3 ± 1
	Model-based	109 ± 5	97 ± 3	5.6 ± 0.1	4 ± 1
Pat 1	NLINV	264 ± 14	56 ± 6	3.0 ± 0.3	55 ± 3
	Model-based	216 ± 11	51 ± 4	2.8 ± 0.2	57 ± 2
Pat 2	NLINV	222 ± 12	82 ± 5	5.3 ± 0.3	18 ± 2
	Model-based	219 ± 6	71 ± 6	4.6 ± 0.4	23 ± 3

[a]Data from Untenberger et al. (18). The results represent mean values ± standard deviation for 10 consecutive heartbeats at 35.7 ms resolution.

an extended gradient-delay correction (unpublished results) and evaluated with an updated software package for automatic vessel segmentation (CAIPI Prototype Software). In more detail, while peak velocities obtained by NLINV and model-based reconstruction reveal excellent agreement, stroke volumes (and cardiac output) which rely on integrated velocities over space and time are slightly lower for model-based reconstructions. This observation reflects the sharper (i.e., smaller) definition of the vessel lumen and must not be considered a flaw but an advantage.

The spatiotemporal improvement achievable by model-based phase-contrast flow MRI may be invested into even faster acquisitions. As already suggested by the numerical simulations presented in Figure 2 and Table 1, Figure 6 advances NLINV and model-based phase-contrast flow acquisitions from seven spokes per image and 35.7 ms total acquisition time (Supporting Videos S3 and S4) to five spokes and 25.6 ms resolution (Supporting Videos S5 and S6). At peak systole, the findings of excellent vessel definition with almost no phase noise and residual streakings confirm the expectations from numerical and experimental validations. Together, these findings clearly support the notion that the use of five spokes represents an extreme but feasible approach to real-time flow MRI at high temporal resolution. This is

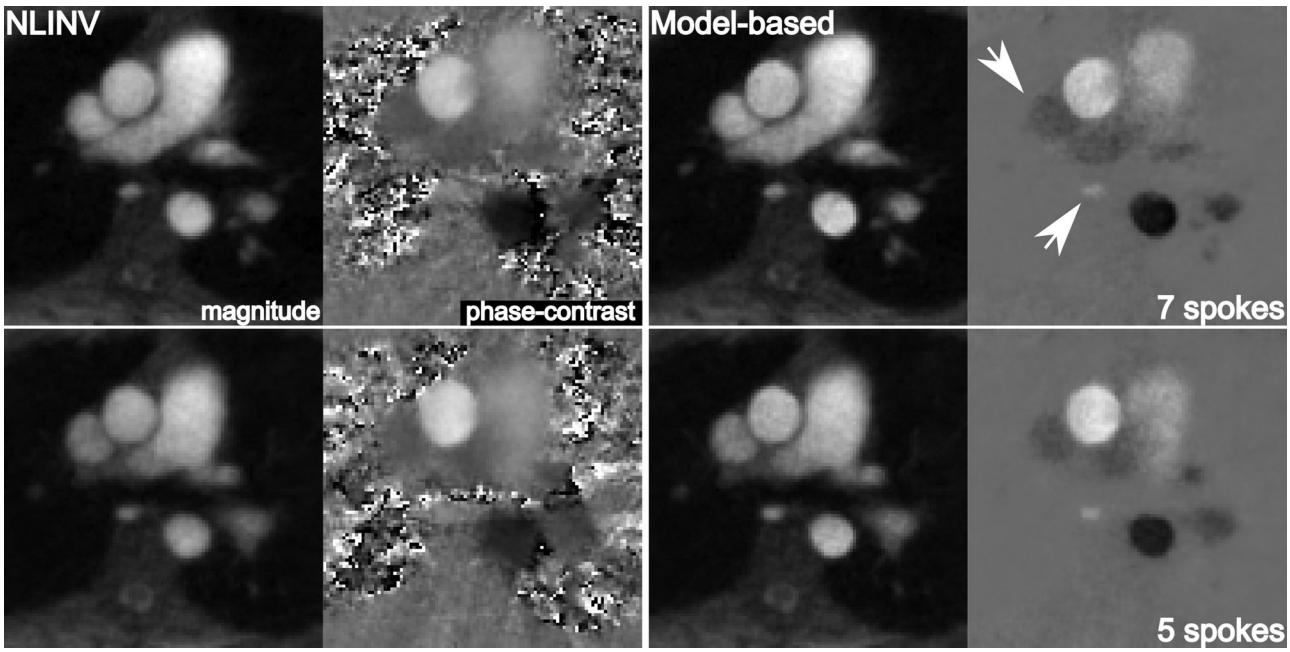

FIG. 6. NLINV (left) and model-based (right) reconstructions of systolic magnitude images and phase-contrast maps (magnified views) for real-time phase-contrast MRI of aortic blood flow (VENC = 200 cm s^{-1}) in a healthy volunteer using seven spokes per frame at 35.7 ms resolution (top) and five spokes at 25.6 ms resolution (bottom). Note the improved delineation of the superior vena cava (upper arrow) and the small azygos vein (lower arrow) in model-based phase-contrast maps.

Table 4
Quantitative Flow Evaluations of Model-Based Reconstructions in the Ascending and Descending Aorta of Healthy Volunteers[a]

		Ascending aorta		Descending aorta	
Subject	Spokes per image	Peak velocity cm s^{-1}	Flow per heartbeat mL	Peak velocity cm s^{-1}	Flow per heartbeat mL
6	7	88 ± 4	96 ± 9	99 ± 5	58 ± 5
	5	89 ± 4	100 ± 4	103 ± 5	70 ± 3
7	7	127 ± 6	107 ± 6	128 ± 5	81 ± 4
	5	116 ± 6	94 ± 5	120 ± 6	68 ± 4
8	7	83 ± 7	77 ± 7	104 ± 4	52 ± 4
	5	84 ± 10	76 ± 7	104 ± 6	55 ± 4
9	7	114 ± 3	106 ± 4	119 ± 3	60 ± 3
	5	115 ± 2	103 ± 5	115 ± 3	60 ± 4
10	7	96 ± 4	81 ± 3	100 ± 5	54 ± 3
	5	96 ± 3	75 ± 4	100 ± 3	54 ± 3
Diff. / %	7 vs 5	−1 ± 4	−4 ± 6	−1 ± 4	2 ± 13

[a]The results represent mean values ± standard deviation for 10 consecutive heartbeats at 35.7 ms and 25.6 ms resolution, respectively. The bottom row presents percentage differences of mean values for acquisitions at 35.7 ms and 25.6 ms resolution.

further confirmed by the quantitative evaluations in Table 4 summarizing peak velocities and flow rates for 5 additional subjects and acquisitions with seven and five spokes. Regardless of possible intrasubject variability in repetitive measurements, mean peak velocities and flow volumes (10 heartbeats) in both the ascending and descending aorta differ by less than 4% when comparing 35.7 ms acquisitions (7 spokes) with 25.6 ms acquisitions (5 spokes).

DISCUSSION

This work demonstrates the successful development and initial description of a novel model-based reconstruction technique for real-time phase-contrast flow MRI and its application to the assessment of cardiovascular blood flow. When compared with a previous flow MRI method based on NLINV reconstructions of two independent flow-compensated and flow-encoded images (18), the flow results are quantitatively accurate, while the images and maps present with improved spatial acuity and reduced residual streaking artifacts. Most importantly, the desired phase-difference maps reveal much reduced phase noise when compared with phase-difference maps of two complex images with arbitrary phases, in particular in areas of low or no MRI signal. As a consequence, the proposed method offers much better access to small vessels such as the azygos vein (see Figure 6). On the other hand, the improved image quality and vessel definition of the model-based phase-contrast method allows for the use of only five spokes per image which pushes real-time flow MRI to a temporal resolution of 25.6 ms or a rate of 39 phase-contrast maps per second. Similar degrees of radial undersampling (i.e., five spokes per image) have already successfully been applied for real-time MRI studies of high-speed tongue movements in elite horn players (37) and experimentally been demonstrated to provide excellent temporal fidelity for a rapid motion phantom (12) when eliminating any temporal filter as done here for the velocity-encoded phase-contrast maps.

At this time, the most relevant limitation of the proposed method is the need for a time-consuming offline calculation. Although conventional NLINV reconstructions are available online for immediate control (18), the nonlinear inverse problem posed by the phase-contrast flow MRI signal model requires new efforts for parallelization, GPU programming and implementation on the existing bypass server to the host computer of our MRI system. Nevertheless, such work will be mandatory to provide an online version for extended clinical trials.

An advantageous extension of the current model-based reconstruction may arise from the fact that the method is applicable to arbitrary trajectories in k-space, and in particular, to different spatial encodings (i.e., sets of spokes) for the flow-encoded and flow-compensated dataset. So far, most if not all phase-contrast MRI acquisition techniques including the one used here, use the same lines in k-space when comparing phase differences between flow-compensated and flow-encoded acquisitions. However, the use of complementary sets of radial spokes, e.g., in two sequential acquisitions, offers at least two advantages: First, it promises to increase the spatial resolution (and computational robustness) of respective model-based reconstructions. This can be seen from the adjoint operator in Eq. [6], where the summation of indices l for $d\rho$ and dz accumulates all available spatial samples. Second, the use of different encodings in k-space, eventually in combination with two similar but sign-inverted bipolar flow-encoding gradients, will allow for a sliding-window approach where model-based reconstructions are shifted by just one dataset (here seven or five spokes) rather than two datasets and thereby improve the effective temporal resolution by a factor of two (here to approximately 18 or 13 ms). Along the same idea, it seems reasonable to extend the model-based concept from one-dimensional (i.e., through-plane) flow to the analysis of phase-contrast MRI studies with three-dimensional velocity encodings.

In conclusion, the present work introduces a novel model-based reconstruction technique for velocity-encoded phase-contrast flow MRI which simultaneously estimates a proton density map, a phase-contrast map and a set of coil sensitivity profiles from each pair of flow-encoded and flow-compensated datasets. The solution to the resulting nonlinear inverse problem is accomplished with the use of the iteratively regularized Gauss-Newton method. When based on highly undersampled

radial FLASH acquisitions, real-time applications benefit from reduced noise and improved spatial accuracy of the computed phase-contrast maps which, therefore, allow for a temporal resolution of 25.6 ms per flow map.

ACKNOWLEDGMENTS

The authors thank Drs. Anja Hennemuth, Teodora Chitiboi, and Markus Hüllebrandt of the Fraunhofer MEVIS Institute for Medical Image Computing, Bremen, Germany, for developing specialized CAIPI software for real-time MRI. We also thank Prof. Dr. Christina Unterberg-Buchwald of the Clinic for Cardiology and Pneumology, University Medical Center Göttingen, Germany, for letting us study her patients. Finally, we are grateful to Dr. Oleksandr Kalentev for numerous discussions and Christian Holme for help with Compute Unified Device Architecture (CUDA) C programming.

REFERENCES

1. Hahn EL. Detection of sea-water motion by nuclear precession. J Geophys Res 1960;65:776–777.
2. Moran PR. A flow velocity zeugmatographic interlace for NMR imaging in humans. Magn Reson Imaging 1982;1:197–203.
3. Van Dijk P. Direct cardiac NMR imaging of heart wall and blood flow velocity. J Comput Assist Tomogr 1984;8:429–436.
4. Bryant DJ, Payne JA, Firmin DN, Longmore DB. Measurement of flow with NMR imaging using a gradient pulse and phase difference technique. J Comput Assist Tomogr 1984;8:588–593.
5. Pelc NJ, Herfkens RJ, Shimakawa A, Enzmann DR. Phase contrast cine magnetic resonance imaging. Magn Reson Q 1991;4:229–254.
6. Gatehouse PD, Keegan J, Crowe LA, Masood S, Mohiaddin RH, Kreitner KF, Firmin DN. Applications of phase-contrast flow and velocity imaging in cardiovascular MRI. Eur Radiol 2005;15:2172–2184.
7. Srichai MB, Lim RP, Wong S, Lee VS. Cardiovascular applications of phase-contrast MRI. AJR Am J Roentgenol 2009;192:662–675.
8. Uecker M, Zhang S, Voit D, Karaus A, Merboldt KD, Frahm J. Real-time MRI at a resolution of 20 ms. NMR Biomed 2010;23:986–994.
9. Uecker M, Hohage T, Block KT, Frahm J. Image Reconstruction by regularized nonlinear inversion – joint estimation of coil sensitivities and image content. Magn Reson Med 2008;60:674–682.
10. Uecker M, Zhang S, Frahm J. Nonlinear inverse reconstruction for real-time MRI of the human heart using undersampled radial FLASH. Magn Reson Med 2010;63:1456–1462.
11. Schätz S, Uecker M. A multi-GPU programming library for real-time applications. In: Algorithms and architectures for parallel processing (Springer). Lect Notes Comp Sci 2012;7439:114–128.
12. Frahm J, Schätz S, Untenberger M, Zhang S, Voit D, Merboldt KD, Sohns JM, Lotz J, Uecker M. On the temporal fidelity of nonlinear inverse reconstructions for real-time MRI – the motion challenge. Open Med Imaging J 2014;8:1–7.
13. Zhang S, Uecker M, Voit D, Merboldt KD, Frahm J. Real-time cardiovascular magnetic resonance at high temporal resolution: radial FLASH with nonlinear inverse reconstruction. J Cardiovasc Magn Reson 2010;12:39–46.
14. Voit D, Zhang S, Unterberg-Buchwald C, Sohns JM, Lotz J, Frahm J. Real-time cardiovascular magnetic resonance at 1.5 T using balanced SSFP and 40 ms resolution. J Cardiovasc Magn Reson 2013;15:79–86.
15. Zhang S, Joseph AA, Voit D, Schätz S, Merboldt KD, Unterberg-Buchwald C, Hennemuth A, Lotz J, Frahm J. Real-time magnetic resonance imaging of cardiac function and flow – recent progress. Quant Imaging Med Surg 2014;4:319–329.
16. Joseph AA, Merboldt KD, Voit D, Zhang S, Uecker M, Lotz J, Frahm J. Real-time phase-contrast MRI of cardiovascular blood flow using undersampled radial fast low-angle shot and nonlinear inverse reconstruction. NMR Biomed 2012;25:917–924.
17. Joseph AA, Kowallick JT, Merboldt KD, Voit D, Schätz S, Zhang S, Sohns JM, Lotz J, Frahm J. Real-time flow MRI of the aorta at a resolution of 40 ms. J Magn Reson Imaging 2014;40:206–213.
18. Untenberger M, Tan Z, Voit D, Joseph AA, Roeloffs V, Merboldt KD, Schätz S, Frahm J. Advances in real-time phase-contrast flow MRI using asymmetric radial gradient echoes. Magn Reson Med 2016;75:1901–1908.
19. Baltes C, Kozerke S, Hansen MS, Pruessmann KP, Tsao J, Boesiger P. Accelerating cine phase-contrast flow measurements using *k-t* BLAST and *k-t* SENSE. Magn Reson Med 2005;54:1430–1438.
20. Kim D, Dynorne HA, Otazo R, Feng L, Sodickson DK, Lee VS. Accelerated phase-contrast cine MRI using *k-t* SPARSE-SENSE. Mag Reson Med 2012;67:1054–1064.
21. Bernstein MA, King FK, Zhou XJ. Handbook of MRI pulse sequences. Burlington, MA: Elsevier Academic Press; 2004.
22. Fessler J. Model-based image reconstruction for MRI. IEEE Signal Process Mag 2010;27:81–89.
23. Block KT, Uecker M, Frahm J. Model-based iterative reconstruction for radial fast spin-echo MRI. IEEE Trans Med Imaging 2009;28:1759–1769.
24. Sumpf TJ, Uecker M, Boretius S, Frahm J. Model-based nonlinear inverse reconstruction for T2 mapping using highly undersampled spin-echo MRI. J Magn Reson Imaging 2011;34:420–428.
25. Sumpf TJ, Petrovic A, Uecker M, Knoll F, Frahm J. Fast T2 mapping with improved accuracy using undersampled spin-echo MRI and model-based reconstructions with a generating function. IEEE Trans Med Imaging 2014;33:2213–2222.
26. Reeder SB, Wen Z, Yu H, Pineda AR, Gold GE, Markl M, Pelc NJ. Multicoil Dixon chemical species separation with an iterative least-squares estimation method. Magn Reson Med 2004;51:35–45.
27. Knopp T, Eggers H, Dahnke H, Prestin J, Sénégas J. Iterative off-resonance and signal decay estimation and correction for multi-echo MRI. IEEE Trans Med Imaging 2009;28:394–404.
28. Liu T, Wisnieff C, Lou M, Chen W, Spincemaille P, Wang Y. Nonlinear formulation of the magnetic field to source relationship for robust quantitative susceptibility mapping. Magn Reson Med 2013;69:467–476.
29. Knoll F, Raya JG, Halloran RO, Baete S, Sigmund E, Bammer R, Block T, Otazo R, Sodickson DK. A model-based reconstruction for undersampled radial spin-echo DTI with variational penalties on the diffusion tensor. NMR Biomed 2015;28:353–366.
30. Kwak Y, Nam S, Akçakaya M, Basha TA, Goddu B, Manning WJ, Tarokh V, Nezafat R. Accelerated aortic flow assessment with compressed sensing with and without use of the sparsity of the complex difference image. Magn Reson Med 2013;70:851–858.
31. Sun A, Zhao B, Li R, Yuan C. Complex-difference constrained reconstruction for accelerated phase contrast flow imaging. In Proceedings of the 23rd Annual Meeting of ISMRM, Toronto, Canada, 2015. Abstract 79.
32. Engl HW, Hanke M, Neubauer A. Regularization of inverse problems. London: Kluwer Academic Publisher; 1996.
33. Bakushinsky AB, Kokurin MY. Iterative methods for approximate solution of inverse problems. Dordrecht: Springer; 2004.
34. Pruessmann KP, Weiger M, Börnert P, Boesiger P. Advances in sensitivity encoding with arbitrary k-space trajectories. Magn Reson Med 2001;46:638–651.
35. Guerquin-Kern M, Lejeune L, Pruessmann KP, Unser M. Realistic analytical phantoms for parallel magnetic resonance imaging. IEEE Trans Med Imaging 2012;31:626–636.
36. Chitiboi T, Hennemuth A, Tautz L, Hüllebrand M, Frahm J, Linsen L, Hahn H. Context-based segmentation and analysis of multi-cycle real-time cardiac MRI. IEEE Int Symp Biomed Imaging 2014;2014:943–946.
37. Iltis PW, Frahm J, Voit D, Joseph AA, Schoonderwaldt E, Altenmüller E. High-speed real-time MRI of fast tongue movements in elite horn players. Quant Imaging Med Surg 2015;5:374–381.

SUPPORTING INFORMATION

Additional Supporting Information may be found in the online version of this article

Video S1. Model-based reconstructions of real-time phase-contrast MRI at 35.7 ms resolution (28 frames per second, seven spokes per image, VENC = 400 cm s^{-1}) of aortic blood flow of a patient with aortic valve insufficiency and partial stenosis: Magnitude images.

Video S2. Model-based reconstructions of real-time phase-contrast MRI at 35.7 ms resolution (28 frames per second, seven spokes per image, VENC = 400 cm s^{-1}) of aortic blood flow of a patient with aortic valve insufficiency and partial stenosis: Phase-contrast maps.

Video S3. Model-based reconstructions of real-time phase-contrast MRI at 35.7 ms resolution (28 frames per second, seven spokes per image, VENC = 200 cm s^{-1}) of aortic blood flow of a young healthy volunteer: Magnitude images.

Video S4. Model-based reconstructions of real-time phase-contrast MRI at 35.7 ms resolution (28 frames per second, seven spokes per image, VENC = 200 cm s^{-1}) of aortic blood flow of a young healthy volunteer: Phase-contrast maps.

Video S5. Model-based reconstructions of real-time phase-contrast MRI at 25.6 ms resolution (39 frames per second, five spokes per image, VENC = 200 cm s^{-1}) of aortic blood flow of a young healthy volunteer: Magnitude images.

Video S6. Model-based reconstructions of real-time phase-contrast MRI at 25.6 ms resolution (39 frames per second, five spokes per image, VENC = 200 cm s^{-1}) of aortic blood flow of a young healthy volunteer: Phase-contrast maps.